Available online at www.sciencedirect.com
SCIENCE DIRECT®
Journal of Computational Physics 202 (2005) 181–195
JOURNAL OF COMPUTATIONAL PHYSICS
www.elsevier.com/locate/jcp

Simulation of fluid slip at 3D hydrophobic microchannel walls by the lattice Boltzmann method ☆

Luoding Zhu [a,*], Derek Tretheway [b], Linda Petzold [a,b], Carl Meinhart [b]

[a] Department of Computer Science, University of California Santa Barbara, Santa Barbara, CA 93106, USA
[b] Department of Mechanical and Environmental Engineering, University of California Santa Barbara, Santa Barbara, CA 93106, USA

Received 15 September 2003; received in revised form 15 April 2004; accepted 5 July 2004
Available online 14 August 2004

Abstract

Fluid slip along hydrophobic microchannel walls has been observed experimentally by Tretheway and Meinhart [Phys. Fluids, 14 (3) (2002) L9]. In this paper, we show how fluid slip can be modeled by the lattice Boltzmann method and investigate a proposed mechanism for the apparent fluid slip [Phys. Fluids (2003)]. By applying an exponentially decaying hydrophobic repulsive force of 4×10^{-3} dyn/cm^3 with a decay length of 6.5 nm, an effective fluid slip of 9% of the main stream velocity is obtained. The result is consistent with experimental μ-PIV data and with the proposed mechanism.
© 2004 Elsevier Inc. All rights reserved.

Keywords: Fluid slip; Slip boundary condition; Hydrophobicity; Microfluidic; Lattice Boltzmann method

1. Introduction

In classical fluid mechanics, the assumption of no-slip at a solid boundary is used as the boundary condition for viscous flows at rigid walls. However, for flows at micro- and nanoscales, this assumption may no longer be accurate. Many researchers have investigated the fluid slip phenomenon [3–12,14,21]. Choi et al. [3] investigated experimentally the slip effects of water flow in hydrophilic/hydrophobic microchannels and found the slip length to vary approximately linearly with the flow shear rate. Lumma et al. [4] measured the flow profile near a wall by double-focus fluorescence cross-correlation; their analysis yields a large apparent fluid slip at the wall. Horn et al. [5] observed the hydrodynamic slippage, which was deduced from thin film

☆ This work was supported by NSF/ITR ACI-0086061.
* Corresponding author.
E-mail address: zhuld@cs.ucsb.edu (L. Zhu).

0021-9991/$ - see front matter © 2004 Elsevier Inc. All rights reserved.
doi:10.1016/j.jcp.2004.07.004

drainage measurements in a solution of nonadsorbing polymer. Watanabe et al. [6,7] found fluid slip at the wall of a hydrophobic duct/pipe with relatively large scale geometry (15×15 mm). Ruckenstein and Rajora [8] studied the fluid slip in a glass capillary with liquid-repellent surfaces. A large slip was inferred at the wall from pressure drop versus flow measurements. Barrat and Bocquet [9] predicted computationally significant slip in nanoporous media. This was confirmed experimentally by Churaev et al. [10]. Zhu and Granick [11] studied experimentally the slip in an oscillating surface force equipment. Pit et al. [12] investigated fluid slip between spinning parallel disks. Thompson and Troian [13] simulated Newtonian liquids under shear, via molecular dynamics. Their result suggested that there is a nonlinear relationship between the magnitude of slip and the local shear rate at a solid surface. For a comprehensive review of fluid slippage over hydrophobic surfaces, see [14] and the references therein. The hydrophobicity phenomena are not well understood. For readers who are interested in hydrophobicity, we refer to the following papers and references therein: [15–21].

Recently, Tretheway and Meinhart [1] measured the velocity profiles of deionized water flowing through a 3D microchannel with a cross-section of 30×300 μm. They found that when the microchannel surface is hydrophilic (the wall attracts water molecules), the conventional assumption of a no-slip boundary condition is valid. However, when the microchannel surface is hydrophobic (the wall repels water molecules), a significant slip (approximately 10% of the free-stream velocity) near the wall was measured. The velocity error in the experimental measurement is within 2%, and the slip length error is within ±0.45 μm.

In this paper, we describe the numerical simulation of the fluid slip on hydrophobic microchannel walls using the lattice Boltzmann method. In the first part of our work, we report computer simulations with the single phase (component) lattice Boltzmann method (LBM) for flow in 3D microchannels, focusing on modeling of the slip boundary condition. In the second part, we address the mechanism of fluid slip with the multiphase (multicomponent) lattice Boltzmann method (the S-C model). We want to point out that, in both cases, we address modeling of the fluid slip generated by hydrophobicity in water flow, *not* the fluid slip generated by *Kn* effects for gas flow.

2. Numerical methods – lattice Boltzmann methods

The lattice Boltzmann method is an alternative to traditional numerical methods for solving incompressible Navier–Stokes equations. Instead of solving for the macroscopic quantities velocity and pressure (or streamfunction and vorticity) directly, LBM deals with the single particle velocity distribution functions $f(\mathbf{x},\boldsymbol{\xi},t)$ ($\mathbf{x}$ represents the spatial coordinates, $\boldsymbol{\xi}$ the particle velocity components, and t is the time variable) based on a simplified Boltzmann equation. For application of the lattice Boltzmann method in the area of microscale flows, see [27,40,41].

In the first part of our work [1] we focus on modeling the slip boundary condition using a 19-discrete velocity lattice Boltzmann model (D3Q19) [28,29]. In the lattice Boltzmann method, the bounce-back scheme is usually used to model the no-slip boundary condition. (We note that the bounce-back scheme can itself also generate slip. An analysis of the slip generated by bounce-back for simple flows can be found in [37]. We found that, on a fine enough grid, the amount of slip caused by the bounce-back scheme alone is negligible compared to the amount observed in experiment. Knudsen number related slip using the bounce-back scheme for microscale flow can be found in [40,41].) It has also been suggested in the literature that specular reflection may be used to model a slip boundary condition. However, the specular reflection scheme used in our work resulted in 100% slip of the fluid on the walls. Instead, we have employed a com-

[1] Preliminary results have been presented at the 2002 ASME International Mechanical Engineering Congress & Exposition, New Orleans, Louisiana, November, 2002. See [25].

bination of bounce-back and reflection to simulate the slip boundary condition. Thus, the slip boundary condition is modeled by assigning a probability of q for bounce-back and $1 - q$ for specular reflection when a particle velocity distribution function $f_j(\mathbf{x},t)$ hits a wall (100% bounce-back if $\boldsymbol{\xi}_j$ is perpendicular to a wall). By varying the value of q, different slip boundary conditions may be modeled. An obvious shortcoming of this approach is its lack of predictability of the amount of slip. A similar scheme has been used by Succi [55] to study slip motion at fluid solid interfaces with heterogeneous catalysis. Such an idea was mentioned in [34,35], and can be dated back to 1867 when Maxwell studied the microscopic modeling of the solid boundary [42]. It was once used in [43] to treat the *no-slip* boundary condition in the lattice gas method, and has also been mentioned in the context of direct simulation Monte Carlo (DSMC) [44]. (In DSMC, specular reflection is combined with the full diffusion condition.) The combination of bounce-back and specular reflection is difficult to implement in a complex geometry. A method for addressing that issue has been proposed in [45].

In the second part of our work, we make use of the multicomponent lattice Boltzmann method [49–52] to investigate a possible mechanism [2] for generating the apparent fluid slip on a hydrophobic wall. The general idea of the mechanism is as follows. The water used in the laboratory experiment was not degased and contains a small amount of absorbed gas. The hydrophobic wall may repel the water molecules within a region very close to the wall but is neutral to water vapor and air molecules. As a result, the water density near the wall may decline, creating a depleted layer very close to the wall. Thus, a thin layer of water–air/water vapor mixture with significantly different water and air/water vapor densities (compared to the well-mixed air–water under standard conditions) may form in the region very near to the wall. Because the vapor density is much smaller than that of water, the average density of the thin layer declines compared to the average mixture density elsewhere. Since the pressure drop between the inlet and outlet that drives the flow can be treated as approximately constant on cross-sections of the inlet and outlet, the thin layer may move faster than the usually mixed water–air (e.g., in the case of a hydrophilic wall), which may result in apparent slip on the hydrophobic wall.

We tested the above proposition by simulating the water–air/water vapor two-phase system with the multicomponent lattice Boltzmann method for flow in a 3D hydrophobic microchannel. The hydrophobic walls were modeled by applying forces in a region very close to the walls. These forces are repulsive to the water molecules, and are neutral to the air/water vapor molecule distribution functions. These forces exponentially decay away from the wall. The initial water–air mixture is assumed to be uniform. The initial density of the air in the water is calculated under standard conditions (at 20 °C and 1 atm). The multicomponent lattice Boltzmann model we use is the S-C model, see [49–52], except that we introduced the additional hydrophobic wall forces into the formulation. The wall force term was inserted into the right-hand side of the equations which are used to update the velocities for computing the new equilibrium velocity distributions.

Numerous researchers have examined hydrophobic surfaces and the related forces. While the effects of hydrophobic forces have been observed, the form and magnitude of the hydrophobic force is not well understood. As a first approximation, we modeled the hydrophobic force as a simple exponential decay with a magnitude and a decay length. A similar force function was explored by Vinogradova [21]. We set the magnitude and decay length to be consistent with experimental observations. The decay length is consistent with the experimental lengthscales at reduced viscosity layer (5 nm) [23,16] or nanobubbles (10–30 nm) [22], as well as the value assumed by Vinogradova (decay length 5–10 nm) [21]. The magnitude is three orders smaller than that assumed by Vinogradova [21].

2.1. Single component lattice Boltzmann method

The LBMs used in our work are in the first part the single phase isothermal LBGK model [28,29], and in the second part the multiphase S-C model [49,50].

The lattice Boltzmann method is a numerical technique to solve a simplified Boltzmann equation – the LBGK model [28,29]

$$\frac{\partial f(\mathbf{x},\boldsymbol{\xi},t)}{\partial t}+\boldsymbol{\xi}\cdot\frac{\partial f(\mathbf{x},\boldsymbol{\xi},t)}{\partial \mathbf{x}}=-\frac{1}{\tau}(f(\mathbf{x},\boldsymbol{\xi},t)-f^0(\mathbf{x},\boldsymbol{\xi},t)), \tag{1}$$

where τ is the relaxation time and f^0 is the equilibrium distribution function. The term $-(1/\tau)(f-f^0)$ is the well-known BGK approximation [30] to the complex collision operator in the Boltzmann equation. The particle velocity space $\boldsymbol{\xi}$ can be discretized by a finite set of velocities, $\{\boldsymbol{\xi}_j, j=0,1,2,\ldots n\}$ (in our case, $n=19$). Let $f_j(\mathbf{x},t)$ be the distribution function for $\boldsymbol{\xi}_j$. Then we have

$$\frac{\partial f_j(\mathbf{x},t)}{\partial t}+\boldsymbol{\xi}_j\cdot\frac{\partial f_j(\mathbf{x},t)}{\partial \mathbf{x}}=-\frac{1}{\tau}(f_j(\mathbf{x},t)-f_j^0(\mathbf{x},t)). \tag{2}$$

After discretization in time, the lattice Boltzmann equation (LBE) is obtained

$$f_j(\mathbf{x}+\boldsymbol{\xi}_j,t+1)=f_j(\mathbf{x},t)-\frac{1}{\tau}(f_j(\mathbf{x},t)-f_j^0(\mathbf{x},t)), \tag{3}$$

where the term $-(1/\tau)(f_j-f_j^0)$ represents collision (note that collision is implicitly defined in LBM, in contrast with molecular dynamics or direct simulation Monte Carlo). Beginning with the initial equilibrium distribution and the distribution at time $t=0$, which can be taken as the initial equilibrium distribution, the one-step computation (from time t to time $t+1$) can be divided into two substeps: (1) compute the collision and update the distribution at time t by summing the collision term and the pre-collision distribution; (2) compute the distribution at time $t+1$ by streaming the post-collision distribution, i.e. the computed right hand side of the LBE. The lattice Boltzmann equation can be treated as a second order discretization both in time and space by the finite difference method of the LBGK equation. Any high order discretization will lose the clear physical interpretation mentioned above.

An intuitive way to see the connection between the lattice Boltzmann equation and the LBGK model is as follows. Following the theory of characteristics for hyperbolic partial differential equations, let $\boldsymbol{\xi}=\mathrm{d}\mathbf{x}/\mathrm{d}t$. The LBGK equation becomes

$$\frac{\mathrm{d}f(\mathbf{x},t)}{\mathrm{d}t}=-\frac{1}{\tau}(f(\mathbf{x},t)-f^0(\mathbf{x},t)). \tag{4}$$

Note that (4) is an ordinary differential equation along the particle trajectory in space $(\mathbf{x},t)$, i.e. (4) an ODE in a Lagrangian coordinate. The projection of the trajectory on space $\mathbf{x}$ is $\boldsymbol{\xi}=\mathrm{d}\mathbf{x}/\mathrm{d}t$. After replacing the total derivative in (4) by a finite difference (forward Euler method), noting that the discretization is done in a Lagrangian coordinate system and that δt can be absorbed by τ, the LBE (3) is recovered. For a rigorous derivation of the LBE from the lattice Boltzmann BGK model, see [35,36,38].

With the new distribution functions obtained, the macroscopic quantities density $\rho(\mathbf{x},t)$ and momentum $\rho\mathbf{u}(\mathbf{x},t)$ can be calculated at each node by

$$\rho(\mathbf{x},t)=\sum_j f_j(\mathbf{x},t), \tag{5}$$

$$(\rho\mathbf{u})(\mathbf{x},t)=\sum_j \boldsymbol{\xi}_j f_j(\mathbf{x},t). \tag{6}$$

We use a standard 3D lattice $D3Q19$ which has 19 discrete particle velocities and can be written as follows:

$$\boldsymbol{\xi}_j=\begin{cases}(0,0,0), & j=0,\\ (\pm1,0,0),(0,\pm1,0),(0,0,\pm1), & j=1,2,\ldots,6,\\ (\pm1,\pm1,0),(\pm1,0,\pm1),(0,\pm1,\pm1), & j=7,8,\ldots,18.\end{cases}$$

For isothermal fluids, the equilibrium distribution function f_j^0 (which is a function of ρ and $\mathbf{u}$) in the $D3Q19$ lattice can be computed via

$$f_j^0(\mathbf{x},t) = \rho(\mathbf{x},t)w_j\left(1 + 3\boldsymbol{\xi}_j\cdot\mathbf{u}(\mathbf{x},t) + \frac{9}{2}(\boldsymbol{\xi}_j\cdot\mathbf{u}(\mathbf{x},t))^2 - \frac{3}{2}\mathbf{u}\cdot\mathbf{u}\right), \tag{7}$$

where w_j is the weight, which takes the values:

$$w_j = \begin{cases} 1/3, & j = 0, \\ 1/18, & j = 1,2,\ldots,6, \\ 1/36, & j = 7,8,\ldots,18. \end{cases}$$

We use the conventional bounce-back scheme to model the no-slip boundary condition. We use a combination of bounce-back and specular refection to model the slip boundary condition; that is, when a particle velocity distribution function f_j hits a wall, f_j is bounced back with probability q, and is reflected with probability $1 - q$. Any f_j which hits a wall along its normal direction is bounced back. The reflected distribution function, f_j, goes towards a neighboring node which is $\pm\delta x$ away from the original node, and updates the distribution function at the neighboring node along the direction it is reflected. In our simulation, both the bounce-back and reflection are executed when a distribution function is halfway between its original site and a wall. Otherwise, the order of accuracy may suffer near the boundaries. Except for modeling of the slip boundary condition, the single component LBM used in our simulation is the lattice BKG D3Q19 model. Readers interested in LB methods can see [31–33,35,36,39,56] and the references therein. We want to point out that the concepts of bounce-back and specular reflection may not have direct physical analogs for liquids. They are used here as an idealization and simplification of the physics. The probabilities of bounce-back and reflection are a ramification of the computation. They are not based directly on experimental or physical results.

2.2. Multi-component lattice boltzmann method

There currently exist several versions of the multicomponent lattice Boltzmann method: the R-K model [46,47], the S-C model [48–51], Swift [57], He [58], Seta [59], Inamuro [60], Luo [61]. The S-C model has been tested in the static case by Hou et al. [53] and Niimura [63]. It has been successfully applied to simulate droplet deformation under shear flow in a 3D channel, see Xi and Duncan [62]. Here in our work it is used to simulate multiphase flow with two components. For each fluid component σ (σ = 0,1 in our case), a single particle velocity distribution function $f^\sigma(\mathbf{x},\boldsymbol{\xi},t)$ is introduced, which solves the LBGK model for that component

$$\frac{\partial f^\sigma(\mathbf{x},\boldsymbol{\xi},t)}{\partial t} + \boldsymbol{\xi}\cdot\frac{\partial f^\sigma(\mathbf{x},\boldsymbol{\xi},t)}{\partial \mathbf{x}} = -\frac{1}{\tau^\sigma}(f^\sigma(\mathbf{x},\boldsymbol{\xi},t) - f^{\sigma(0)}(\mathbf{x},\boldsymbol{\xi},t)). \tag{8}$$

Here τ^σ and $f^{\sigma(0)}$ are the relaxation time and the equilibrium distribution function for component σ, respectively.

After discretization in particle velocity space $\boldsymbol{\xi}$ and in time t, we get the multicomponent LBE

$$f_j^\sigma(\mathbf{x}+\boldsymbol{\xi}_j, t+1) = f_j^\sigma(\mathbf{x},t) - \frac{1}{\tau^\sigma}(f_j^\sigma(\mathbf{x},t) - f_j^{\sigma(0)}(\mathbf{x},t)), \tag{9}$$

where f_j^σ is the distribution function for the σ component along the direction $\boldsymbol{\xi}_j$. Note that the discretization in $\boldsymbol{\xi}$ is the same for each component.

One important new feature for the multicomponent lattice Boltzmann model is the introduction of an interparticle interaction potential, which is defined as

$$V(\mathbf{x},\mathbf{y}) = \sum_{\sigma}\sum_{\sigma'} G_{\sigma\sigma'}(\mathbf{x},\mathbf{y})\psi^{\sigma}(\mathbf{x})\psi^{\sigma'}(\mathbf{y}). \tag{10}$$

Here the Greens function, $G_{\sigma\sigma'}(\mathbf{x},\mathbf{y})$, characterizes the nature of the interaction between different components (attractive or repulsive and its strength). The choice of ψ determines the equation of state of the system under study. By selecting different G and ψ, various fluid mixtures and multiphase flows can be simulated. If only the nearest neighbor interactions are considered, the Greens function G can be put into the following form:

$$G_{\sigma\sigma'}(\mathbf{x},\mathbf{y}) = \begin{cases} 0, & |\mathbf{x}-\mathbf{y}| > c, \\ g_{\sigma\sigma'}, & |\mathbf{x}-\mathbf{y}| = c, \end{cases}$$

where $c = \delta x/\delta t$ is the lattice speed. Here δx is the spatial width along the $\boldsymbol{\xi}$ direction, and δt is the time step. In our case, $c = 0$ for $j = 0$, $c = 1$ for $j = 1,2,3,4,5,6$ and $c = \sqrt{2}$ for the other directions. $g_{\sigma\sigma'}$ is a symmetric matrix that specifies the interaction of different components along each direction.

The equilibrium distribution $f_j^{\sigma(0)}$ can be written as

$$f_j^{\sigma(0)}(\mathbf{x},t) = \rho^{\sigma}(\mathbf{x},t)w_j\left(1 + 3\boldsymbol{\xi}_j\cdot\mathbf{u}^{\sigma}(\mathbf{x},t) + \frac{3}{2}\left(3\boldsymbol{\xi}_j\boldsymbol{\xi}_j : \mathbf{u}^{\sigma}(\mathbf{x},t)\mathbf{u}^{\sigma}(\mathbf{x},t) - \mathbf{u}^{\sigma}(\mathbf{x},t)\cdot\mathbf{u}^{\sigma}(\mathbf{x},t)\right)\right), \tag{11}$$

where w_j is the weight, as in the single component case. The mass density of component σ is defined by

$$\rho^{\sigma}(\mathbf{x},t) = \sum_j m^{\sigma} f_j^{\sigma}(\mathbf{x},t), \tag{12}$$

where m^{σ} is the molecular mass of component σ. The velocity, $\mathbf{u}^{\sigma}$, is computed via

$$\rho^{\sigma}(\mathbf{x},t)\mathbf{u}^{\sigma}(\mathbf{x},t) = \rho^{\sigma}(\mathbf{x},t)\bar{\mathbf{u}}(\mathbf{x},t) + \tau^{\sigma}\frac{\mathrm{d}p^{\sigma}}{\mathrm{d}t}(\mathbf{x},t) + \tau^{\sigma}\mathbf{h}^{\sigma}(\mathbf{x}), \tag{13}$$

where the average velocity $\bar{\mathbf{u}}$ is defined by

$$\bar{\mathbf{u}}(\mathbf{x},t)\sum_{\sigma}\frac{\rho^{\sigma}(\mathbf{x},t)}{\tau^{\sigma}} = \sum_{\sigma}\left(\frac{m^{\sigma}}{\tau^{\sigma}}\sum_j f_j^{\sigma}(\mathbf{x},t)\boldsymbol{\xi}_j\right). \tag{14}$$

Here $\mathrm{d}p^{\sigma}/\mathrm{d}t$ is the net rate of momentum change that can be computed in terms of the interaction potential

$$\frac{\mathrm{d}p^{\sigma}}{\mathrm{d}t}(\mathbf{x},t) = -\sum_{\mathbf{y}}\nabla_{\mathbf{y}}V(\mathbf{x},\mathbf{y}) = -\psi^{\sigma}(\mathbf{x})\sum_{\sigma'}\sum_j G_{\sigma\sigma'}^{j}\psi^{\sigma'}(\mathbf{x}+\boldsymbol{\xi}_j)\boldsymbol{\xi}_j. \tag{15}$$

Note that here the Greens function depends on the direction $\boldsymbol{\xi}_j$. This is because the original S-C model was formulated on a 4D face-centered hyper-cube (FCHC) lattice. When projecting the 4D FCHC lattice onto the D3Q19 lattice, the nearest neighbors in the 4D FCHC lattice correspond to the nearest and next nearest neighbors in the D3Q19 lattice.

The forces $\boldsymbol{h}(\mathbf{x})$ that we introduce to model the hydrophobic walls are added to the right-hand side of the equations which are used to compute the $\mathbf{u}^{\sigma}$. Our choice of $\mathbf{h}^{\sigma}(\mathbf{x})$ is as follows: (index 0 denotes the fluid in the model to simulate the water and index 1 the fluid to simulate the air/water vapor)

$$\mathbf{h}^1(\mathbf{x}) = 0,$$

$$\mathbf{h}^0(\mathbf{x}) = (0, g_2(y), g_3(z)),$$

$$g_2(y) = \pm g_{2_0}\exp(-y/\lambda),$$

$$g_3(z) = \pm g_{3_0}\exp(-z/\lambda),$$

where y is the distance away from the side walls along the inward normal direction, and z has a similar meaning for the top and bottom walls. The λ can be determined by specifying the distance away from the wall (y_0 and z_0) where the force diminishes to 1% of the maximum magnitude (g_{2_0} and g_{3_0}) at the wall: $0.01 g_{2_0} = g_{2_0}\exp(-y_0/\lambda)$. In the present simulation, the parameters were chosen as follows: $g_{2_0} = g_{3_0} = 0.2$ (4×10^{-3} dyn/cm^3 in dimensional form. We address this choice in Section 3), $y_0 = 30$ nm, $z_0 = 30$ nm. The decay length is $\lambda = 6.5$ nm

$$\psi^\sigma = \rho^\sigma,$$
$$G^j_{\sigma\sigma'} = \begin{bmatrix} 0 & 0.2 \\ 0.2 & 0 \end{bmatrix} \quad \text{for } j = 0, 1, \ldots, 6,$$
$$G^j_{\sigma\sigma'} = \begin{bmatrix} 0 & 0.1 \\ 0.1 & 0 \end{bmatrix} \quad \text{for } j = 7, 8, \ldots, 18.$$

These choices of ψ and G have been used in the literature, in the simulation of bubbles in fluids [49,52,53]. The values of y_0 and z_0 were chosen to be consistent with the bubble heights observed experimentally by Tyrell and Attard [22].

The macroscopic quantities are connected to distribution functions by the following relations:

$$\rho(\mathbf{x}, t) = \sum_\sigma \rho^\sigma(\mathbf{x}, t), \tag{16}$$

$$(\rho\mathbf{u})(\mathbf{x}, t) = \sum_\sigma m^\sigma \sum_j f_j^\sigma \boldsymbol{\xi}_j + \frac{1}{2}\sum_\sigma \frac{\mathrm{d}p^\sigma}{\mathrm{d}t}(\mathbf{x}, t). \tag{17}$$

The dimensionless viscosity of the system is defined by

$$v = \frac{\sum_\sigma \frac{2\rho^\sigma \tau^\sigma}{\rho} - 1}{6}. \tag{18}$$

3. Simulation results

3.1. Single component lattice Boltzmann simulation

In the first part of our work, we closely followed the parameters in the experiment [1], except that the length of the channel was decreased from 8.25 cm in the experiment to 600 μm in the simulation. In the simulation, the length of the channel (600 μm) was twice the width of the channel (300 μm). The shorter channel length is justified because a periodic boundary condition is used along the channel direction. See Fig. 1 for a diagram of the 3D microchannel used in the simulation. The microchannel length direction is denoted as the x direction (600 μm in the simulation), the width as the y direction (300 μm in the simulation), and the depth as the z direction (30 μm in the simulation). In all the figures presented below, the velocity profile plotted was taken on the cross-section $x = 300$ μm at a plane with $z = 15$ μm normal to the cross-section as a function of y, or at a plane with $y = 150$ μm normal to the cross-section as a function of z, depending on the context. The simulation presented here uses a spatial discretization with resolution $400 \times 200 \times 20$ (x, y, z directions, respectively).

We performed simulations on a series of gradually refined grids. The number of nodes in the z direction was $10, 15, 20, 25, 30, 35$. The lattice Boltzmann simulations on different grids were performed according to the paper [54]. We found that the fluid slip percentage was convergent as the grid was refined. We also computed the quantity $\|u_{2h} - u_{4h}\|_{L2}/\|u_h - u_{2h}\|_{L2}$ (where h is the grid spacing) on three successively refined grids

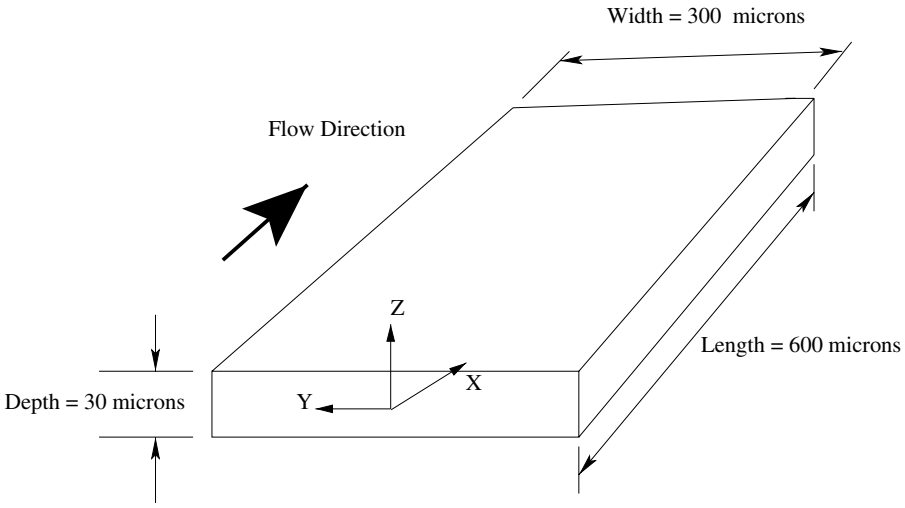

Fig. 1. The demonstration of the 3D micro-channel for single component lattice Boltzmann simulation.

with refinement ratio 2: $100 \times 50 \times 5$, $200 \times 100 \times 10$ and $400 \times 200 \times 20$. The ratio was 3.89. This indicates that the numerical method is of second order in space, as claimed in the literature. Due to computational limitations, we did not check this on finer grids. Instead, we compared the velocity field presented in our paper to those computed from a series of finer grids ($500 \times 250 \times 25$, $600 \times 300 \times 30$, $700 \times 350 \times 35$), and found that they are almost indistinguishable.

The simulation was performed on the PC-cluster of the Computer Science Department at UCSB. The cluster has 33 dual-processor (Intel Xeon) nodes that are connected by 1 GB copper. Each node has a memory of 3 GB and each processor has a speed of 2.6 GHz. The lattice Boltzmann models we used were parallelized by domain decomposition and MPI. See [24] for details. The simulation was run until the flow reached steady state (approximately 500,000 steps). The conventional bounce-back scheme in LBM was applied to model the no-slip boundary condition, while a combination of bounce-back and reflection was employed to simulate the slip boundary condition.

In the no-slip case, our numerical solution matches very well the exact solution of Stokes flow assuming a no-slip boundary condition [26], and also agrees well with the experimental result. Fig. 2 shows the velocity profiles in the case of hydrophilic walls. The profile is taken at the cross-section $x = 300$ μm with the z coordinate equal to 15 μm. The x-axis is the normalized velocity, and the y-axis is the distance from the wall (unit: micron). The squares are the experimental data, the dashed line is the exact solution, and the solid line is the LBM simulation result. We can see that our simulation result is almost indistinguishable from the exact solution and matches well with the experimental data.

In the slip scenario, our numerical velocity profile agrees well with that of the experiment. A slip of about 10% on the wall was attained by assigning the probability of bounce-back to 0.03 and of reflection to 0.97 when the velocity distribution function hits the wall. See Fig. 3 for velocity profiles in the case of hydrophobic walls. The profile is taken at the cross-section $x = 300$ μm with the z coordinate equal to 15 μm. The x-axis is the normalized velocity and the y-axis is the position from the wall. The triangles represent experimental data. The solid line is the LBM simulation result. We can see that our numerical result agrees reasonably well with the experimental data.

In Fig. 4, both velocity profiles along the y and z directions were plotted together. The profiles are taken at the cross-section $x = 300$ μm with the z coordinate equal to 15 μm as a function of y, and with the y

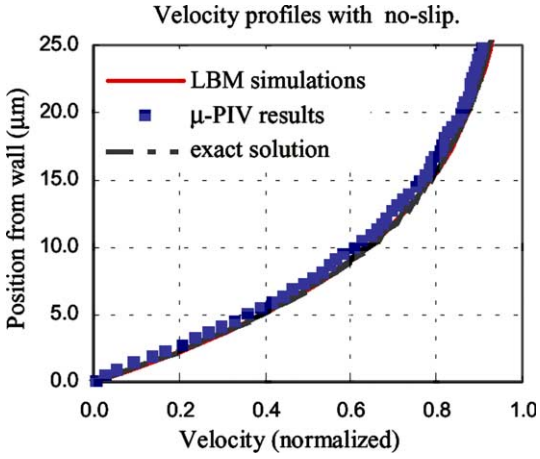

Fig. 2. Velocity profiles in the case of hydrophilic walls. The profile is taken at the cross-section $x = 300$ μm with the z coordinate equal 15 μm. The x-axis is the normalized velocity and the y-axis is the distance from the wall (unit: micron). The squares are the experimental data, the dashed line is the exact solution, and the solid line is the LBM simulation result.

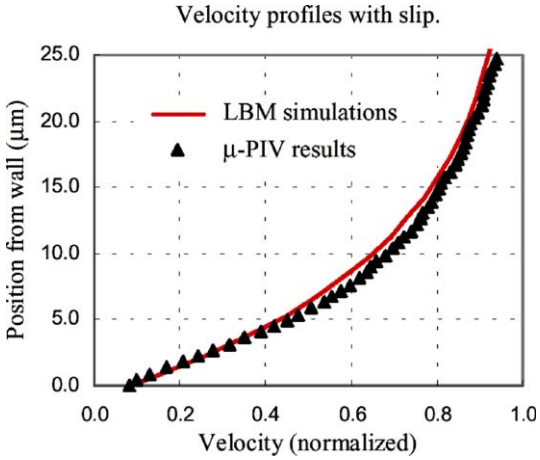

Fig. 3. Velocity profiles in the case of hydrophobic walls. The profile is taken at the cross-section $x = 300$ μm with the z coordinate equal to 15 μm. The x-axis is the normalized velocity and the y-axis is the position from the wall. The triangles represent experimental data. The solid line is the LBM simulation result.

coordinate equal to 150 μm as a function of z. The x-axis is the normalized velocity and the y-axis is the distance from the walls, normalized by the depth and width of the channel, respectively. The solid line is the profile along the y direction, and the curve plotted by triangles is the profile along the z direction. We can see that the fluid slip in the z direction (channel depth) is slightly larger than the slip in the y direction (channel width). Experimental data are not available for the velocity profile along the depth direction.

Fig. 5 shows the slip length as a function of location along the width direction and the depth direction. Fig. 5(a) plots fluid slip length at the top or bottom walls as a function of distance from the side wall along the width direction, and Fig. 5(b) plots fluid slip length at the side walls as a function of distance from the bottom wall along the depth direction. We see that the variation of slip length along the side walls (separated by 300 μm) is significantly different from the variation of slip length along the bottom and top walls

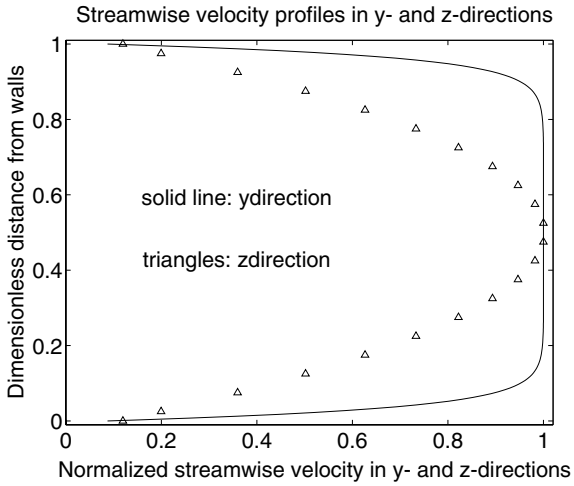

Fig. 4. Velocity profiles in the case of hydrophobic walls. The profiles are taken at the cross-section $x = 300$ μm with the z coordinate equal to 15 μm as a function of y (solid line), and with the y coordinate equal to 150 μm as a function of z (△). The x-axis is the normalized velocity and the y-axis is the distance from the walls, normalized by the depth and width of the channel, respectively.

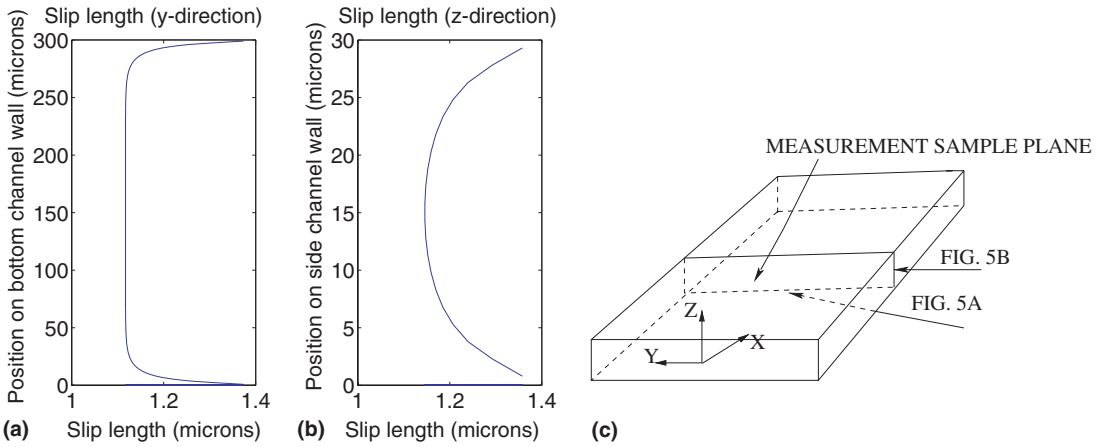

Fig. 5. (a) and (b) depict how the fluid slip length varies along the perimeter of the channel at streamwise position of $x = 300$ μm. (a) Variation of slip length as a function of y along the top or bottom wall. (b) Variation of slip length as a function of z along the side channel walls. (c) Measurement sample plane and the locations of slip length plotted in (a) and (b).

(separated by 30 μm). However, the magnitudes are similar, ranging between 1.1 and 1.4 μm. Fig. 5(c) shows the measurement sample plane and the locations of slip length plotted in Figs. 5(a) and (b).

3.2. Multi-component lattice Boltzmann simulation

In the second part of our work, we investigated a possible generating mechanism for apparent fluid slip [2], via the multi-component lattice Boltzmann method (the S-C model). We performed the simulation on a $0.1 \times 1 \times 2$ μm^3 microchannel. The grid spacing is 5 nm. The non-dimensional hydrophobic wall force used in the simulation is 0.2, corresponding to a physical force of 4×10^{-3} dyn/cm^3 with a decay length of 6.5

nm, as was specified in Section 2. The appropriate magnitude of this force is not well defined. However, Vinogradova [21] modeled attractive hydrophobic interactions as a decaying exponential with a magnitude of 1 dyn and a decay length of between 5 and 15 nm. For the current simulation, the force function was chosen so that the simulation results would be consistent with experimental observations. While the decay length, $\lambda = 6.5$ nm, is consistent with the values of Vinogradova [21], the magnitude of the hydrophobic force, 4×10^{-3} dyn, is significantly lower. The difference may arise from possible non-uniformities in the hydrophobic OTS coatings in the microchannels. This repulsive hydrophobic force causes the density of the synthetic fluid used to simulate water in the multi-component lattice Boltzmann simulation to be greater than 1. We rescaled the density to 1 for the fluid used to model water by the maximum density in the simulation result (about 1.07).

We performed simulations on a series of gradually refined grids. The number of nodes in the z direction was $10, 15, 20, 25, 30$. We found that the fluid slip percentage was convergent as the grid was refined.

Fig. 6 shows the fluid densities as a function of distance away from the side wall at the cross-section $x = 1$ μm and $z = 50$ nm. The x-axis is the density and the y-axis is the distance from the side wall. Fig. 6(a) shows the density of the fluid used to simulate water in the model along the y direction (in the middle of the z direction) on a cross-section in the middle of the channel (x direction). Fig. 6(b) shows the density of the fluid used to simulate water vapor/air. We can see that the density of water is decreased and that of water vapor/air is increased close to the walls. Fig. 7 gives a detailed picture of the density change close to the wall. Sakurai et al. [20] have also observed a drastic decrease of the water molecule number density at a monolayer–water interface from the simulation results of water between hydrophobic surfaces, via molecular dynamics. Our results are consistent with theirs.

Fig. 8 shows the normalized streamwise velocity profile and a local blowup along the y direction at cross-section $x = 1$ μm for $z = 50$ nm. The x-axis is the normalized velocity, and the y-axis is the position from the side wall (unit: micron). The solid line (in (a) and (b)) is the velocity profile when no wall forces are present.

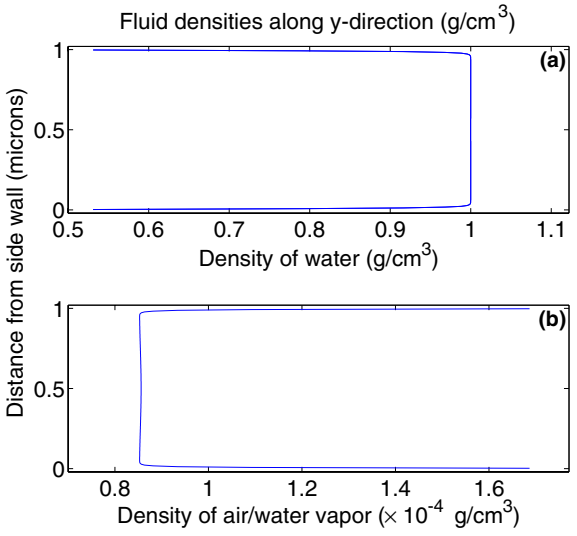

Fig. 6. Normalized fluid densities as a function of distance away from the side wall at the cross-section $x = 1$ μm and $z = 50$ nm. The x-axis is the density of water or air/water vapor, and the y-axis is the distance from the side wall. The graph (a) is the density profile for water and the graph (b) is the density profile for air/water vapor.

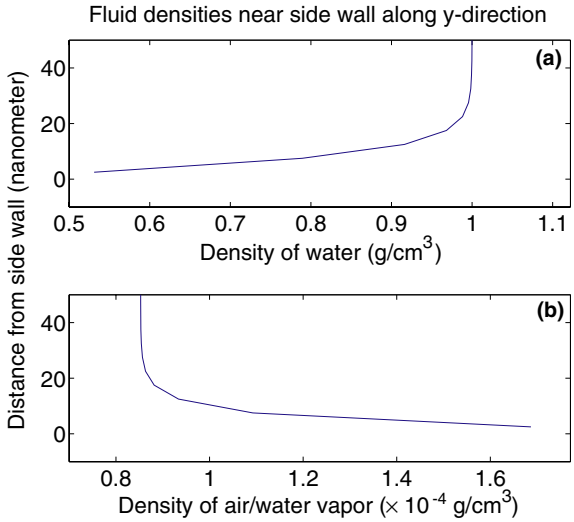

Fig. 7. Fluid density variation depicted in Fig. 6. The 50 nm region close to the side wall is shown.

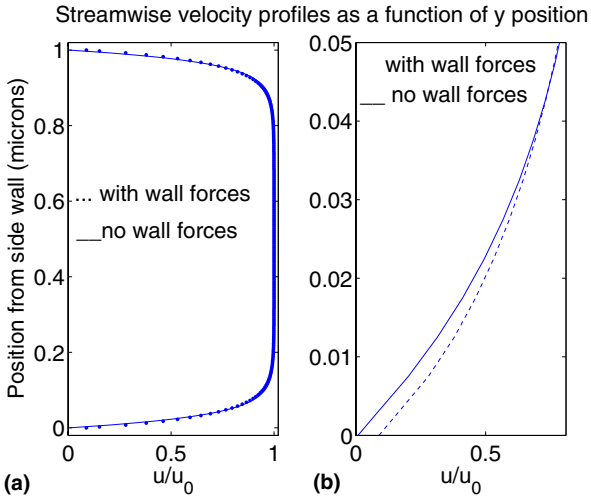

Fig. 8. Normalized streamwise velocity profiles along the y direction at cross-section $x = 1$ μm for $z = 50$ nm. The solid lines are the velocity profiles when no wall forces are used. The dotted or dashed line is the case where wall forces are introduced. The graph (a) is normalized velocity at $z = 50$ nm as a function of distance from the side wall (y direction). The graph (b) shows the normalized velocity profile near the side channel wall.

The dotted line (in part (a)), or the dashed line (in part (b)) is the case where wall forces are introduced. In contrast to the former case, the latter results in apparent slip at the walls. (See Fig. 8(b) for the local blowup near the side wall.) We can see from Figs. 6–8 that in the region very close to the walls, the water density decreases and the water vapor/air density rises. This enables the fluid slip on the walls (approximately 9% of free stream velocity) compared to the solid lines in Fig. 8, which illustrate the case where no hydrophobic wall forces were applied.

4. Summary and discussion

With the single phase lattice Boltzmann method (D3Q19 model), we simulated the flow of water in a 3D microchannel with hydrophilic/hydrophobic walls. The classic bounce-back scheme was used to model the hydrophilic walls, while a combination of bounce-back and specular reflection was applied to model the partial slip boundary condition at the hydrophobic walls. Good quantitative agreement was observed between the simulations and previous experimental results. In the case of hydrophilic walls, the simulation result agrees almost exactly with the analytic solution. In the case of hydrophobic walls, a 10% slip was attained by assigning the probability of bounce-back to 0.03 and the probability of reflection to 0.97. The value of q is consistent with Succi's work [55]. This seems to indicate that partial fluid slip generated by hydrophobicity may be modeled by a combination of bounce-back and specular reflection. However, it remains to be further verified whether the combination scheme can accurately capture the slip motion caused by hydrophobicity. See [55] for details.

With the multiphase lattice Boltzmann method (the S-C model), we investigated a possible mechanism for fluid slip. Due to computational limitations, the corresponding physical size of the simulation domain was $0.1 \times 1 \times 2$ μm, whereas the experimental results were obtained in a microchannel with a cross-section of 30×300 μm. The hydrophobic walls were modeled by applying an exponentially decaying force of 4×10^{-3} dyn with a decay length 6.5 nm from the wall, which is consistent with the work of Vinogradona [21]. This force repels the water molecules, but has no effect on the air/water vapor molecules. The force produces a slip of approximately 9% of the main stream velocity, which corresponds to the experimental μ-PIV results. It indicates that the presence of a depleted water layer (low density region) near the hydrophobic surface may produce the apparent fluid slip observed experimentally.

Acknowledgment

We thank the following people for their useful conversations and discussions of the lattice Boltzmann method: Shulin Hou, Shiyi Chen, Hudong Chen, Nicos Martys, Xiaobo Nie, and Lishi Luo.

References

[1] D.C. Tretheway, C.D. Meinhart, Apparent fluid slip at hydrophobic microchannel walls, Phys. Fluids 14 (3) (2002) L9.
[2] D.C. Tretheway, C.D. Meinhart, A generating mechanism for apparent fluid slip in hydrophobic microchannels, Phys. Fluids 16 (5) (2004) 1509.
[3] C.H. Choi, K.J.A. Westin, K.S. Breuer, Apparent slip flows in hydrophilic and hydrophobic microchannels (submitted).
[4] D. Lumma, A. Best, A. Gansen, F. Feuillebois, J.O. Radler, O.I. Vinogradova, Flow profile near a wall measured by double-focus fluorescence cross-correlation, Phys. Rev. E 67 (2003) 056313.
[5] R.G. Horn, O.I. Vinogradova, M.E. Mackay, N. Phan-Thien, Hydrodynamic slippage inferred from thin film drainage measurements in a solution of nonadsorbing polymer, J. Chem. Phys. 112 (14) (2000).
[6] K. Watanabe, Yanuar, H. Mizunuma, Slip of Newtonian fluids at solid boundary, JSME Int. J. Ser. B 41 (1998) 525.
[7] K. Watanabe, Yanuar, H. Udagawa, Drag reduction of Newtonian fluid in a circular pipe with a highly water-repellant wall, J. Fluid Mech. 381 (1999) 225.
[8] E. Ruckenstein, P. Rajora, On the no-slip boundary condition of hydrodynamics, J. Colloid Interface Sci. 96 (1983) 488.
[9] J. Barrat, L. Bocquet, Large slip effect at a nonwetting fluid–solid interface, Phys. Rev. Lett. 82 (1999) 4671.
[10] N. Churaev, V. Sobolev, A. Somov, Slippage of liquids over lyophobic solid surface, J. Colloid Interface Sci. 97 (1984) 574.
[11] Y. Zhu, S. Granick, Rate-dependent slip of Newtonian liquid at smooth surfaces, Phys. Rev. Lett. 87 (2001) 096105.
[12] R. Pit, H. Hervet, L. Leger, Direct experimental evidence of slip in hexadecane: solid interfaces, Phys. Rev. Lett. 85 (2000) 980.
[13] P.A. Thompson, S.M. Troian, A general boundary condition for liquid flow at solid surfaces, Nature 389 (6649) (1997) 360–362.
[14] O.I. Vinogradova, Slippage of water over hydrophobic surfaces, Int. J. Miner. Process. 56 (1999) 31–60.

[15] L. Mainbaum, D. Chandler, A coarse-grained model of water confined in a hydrophobic tube, J. Phys. Chem. B 107 (2003) 1189–1193.
[16] K. Lum, D. Chandler, J.D. Weeks, Hydrophobicity at small and large length scales, J. Phys. Chem. B 103 (1999) 4570–4577.
[17] D.M. Huang, D. Chandler, The hydrophobic effect and the influence of solute–solvent attractions, J. Phys. Chem. B 106 (2002) 2047–2053.
[18] N.F. Bunkin, O.A. Kiseleva, A.V. Lobeyev, T.G. Movchan, Effect of salts and dissolved gas on optical cavitation near hydrophobic and hydrophilic surfaces, Langmuir 13 (1997) 3024–3028.
[19] D. Chandler, Two faces of water, Nature 417 (2002) 491.
[20] M. Sakurai, H. Tamagawa, K. Ariga, T. Kunitake, Y. Inoue, Molecular dynamics simulation of water between hydrophobic surfaces. Implication for the long-range hydrophobic force, Chem. Phys. Lett. 289 (1998) 567.
[21] O.I. Vinogradova, Possible implications of hydrophobic slippage on the dynamic measurements of hydrophobic forces, J. Phys.: Condens. Matter 8 (1996) 9491.
[22] J. Tyrell, P. Attard, Images of nanobubbles on hydrophobic surfaces and their interactions, Phys. Rev. Lett. 87 (2001) 176104.
[23] D. Schwendel, T. Hayashi, R. Dahint, A. Pertsin, M. Grunze, R. Steitz, F. Schreiber, Interaction of water with self-assembled monolayers: neutron reflectivity measurements of the water density in the interface region, Langmuir 19 (2003) 2284–2293.
[24] L. Zhu, J. Zhou, L. Petzold, T. Yang, Parallel simulation of fluid slip at hydrophobic microchannel walls by the multi-component lattice Boltzmann method, in: SIAM Conference on Parallel Processing for Scientific Computing, San Francisco, CA, February 25–27, 2004.
[25] D.C. Tretheway, L. Zhu, L.R. Petzold, C.D. Meinhart, Examination of the slip boundary condition by μ-PIV and lattice Boltzmann simulation, in: 2002 ASME International Mechanical Engineering Congress & Exposition, New Orleans, Louisiana, November, 2002.
[26] W. White, Viscous Fluid Flow, McGraw-Hill, New York, 1974.
[27] G.E. Karniadakis, A. Beskok, Micro-flows – Fundamentals and Simulation, Springer, New York, 2002.
[28] Y.H. Qian, Lattice gas and lattice kinetic theory applied to the Navier–Stokes equations, Ph.D. Thesis, University Pierre et Marie Curie, Paris, 1990.
[29] S.Y. Chen, H.D. Chen, D. Martinez, W. Matthaeus, Lattice Boltzmann model for simulation of magnetohydrodynamics, Phys. Rev. Lett. 67 (1991) 3776.
[30] P.L. Bhatnagar, E.P. Gross, M. Krook, A model for collision processes in gases, I: small amplitude process in charged and neutral one-component system, Phys. Rev. 94 (1954) 511.
[31] D.H. Rothman, S. Zaleski, Lattice gas models of phase separation: interface phase, transitions and multiphase flow, Rev. Mod. Phys. 66 (1994) 1417.
[32] S.Y. Chen, G.D. Doolen, Lattice Boltzmann method for fluid flows, Annu. Rev. Fluid Mech. 30 (1998) 329.
[33] L.S. Luo, Unified theory of the lattice Boltzmann models for nonideal gases, Phys. Rev. Lett. 81 (1998) 1618.
[34] L.S. Luo, The future of lattice-gas and lattice Boltzmann methods, in: ICASE/LaRC/NSF/ARO Workshop on Computational Aerosciences in the 21st Century Hampton, Virginia, April 22–24, 1998.
[35] D.A. Wolf-Gladrow, Lattice-gas Cellular Automata and Lattice Boltzmann Models – An Introduction, Springer, Berlin, 2000.
[36] X. He, L.S. Luo, Theory of lattice Boltzmann method: from the Boltzmann equation to the lattice Boltzmann equation, Phys. Rev. E 56 (1997) 6811.
[37] X. He, Q. Zou, L. Luo, M. Dembo, Analytic solutions of simple flows and analysis of nonslip boundary conditions for the lattice Boltzmann BGK model, J. Stat. Phys. 87 (1/2) (1997).
[38] X. He, L. Luo, A priori derivation of the lattice Boltzmann equation, Phys. Rev. E 55 (6) (1997).
[39] S. Hou, Lattice Boltzmann method for incompressible viscous flow, Ph.D. Thesis, Kansas State University, 1995.
[40] X. Nie, G.D. Doolen, S.Y. Chen, Lattice Boltzmann simulations of fluid flows in MEMS, J. Stat. Phys. 107 (1/2) (2002).
[41] C.Y. Lim, C. Shu, X.D. Niu, Y.T. Chew, Application of lattice Boltzmann method to simulate microchannel flows, Phys. Fluids 14 (7) (2002) 2299.
[42] J.C. Maxwell, Philos. Trans. R. Soc. Lond. A 170 (1867) 231.
[43] P. Lavallee, J.P. Boon, A. Noullez, Boundaries in lattice gas flows, Physica D 47 (1991) 233.
[44] G.P. Bird, Molecular Gas Dynamics and the Direct Simulation of Gas Flows, Oxford Science Publications, 1994.
[45] J.G. Zhou, An elastic-collision scheme for lattice Boltzmann methods, Int. J. Mod. Phys. C 12 (3) (2001) 387.
[46] D.H. Rothman, J.M. Keller, Immiscible cellular-automaton fluids, J. Stat. Phys. 52 (1988) 1119.
[47] A.K. Gunstensen, D.H. Rothman, S. Zaleski, G. Zanetti, Lattice Boltzmann model of immiscible fluids, Phys. Rev. A 43 (1991) 4320.
[48] D. Grunau, S.Y. Chen, K. Eggert, A lattice Boltzmann model for multiphase fluid flows, Phys. Fluids A 5 (1993) 2557.
[49] X. Shan, H. Chen, Lattice Boltzmann model for simulating flows with multiple phases and components, Phys. Rev. E 47 (3) (1993) 1815.
[50] X. Shan, H. Chen, Simulation of nonideal gases and liquid–gas phase transitions by the lattice Boltzmann equation, Phys. Rev. E 49 (1994) 2941.

[51] X. Shan, G.D. Doolen, Multicomponent lattice Boltzmann model with interparticle interaction, J. Stat. Phys. 81 (1995) 379.
[52] N.S. Martys, H. Chen, Simulation of multicomponent fluids in complex three-dimensional geometries by the lattice Boltzmann method, Phys. Rev. E 53 (1) (1996) 743.
[53] S. Hou, X. Shan, Q. Zou, G.D. Doolen, W.E. Soll, Evaluation of two lattice Boltzmann models for multiphase flows, J. Comput. Phys. 138 (1997) 695.
[54] J. Sterling, S. Chen, Stability analysis of lattice Boltzmann Methods, J. Comput. Phys. 123 (1996) 196.
[55] S. Succi, Mesoscopic modeling of slip motion at fluid solid interfaces with heterogeneous catalysis, Phys. Rev. Lett. 89 (6) (2002) 5.
[56] S. Succi, The Lattice Boltzmann Equation, Oxford University Press, Oxford, 2001.
[57] M.R. Swift, W.R. Osborn, J.M. Yeomans, Lattice Boltzmann simulation of nonideal fluids, Phys. Rev. Lett. 75 (1995) 830–833.
[58] X. He, S. Chen, R. Zhang, A lattice Boltzmann scheme for incompressible multiphase flow and its application in simulation of Rayleigh–Taylor instability, J. Comput. Phys. 152 (1999) 642–663.
[59] T. Seta, K. Kono, S. Chen, Lattice Boltzmann method for two-phase flows, Int. J. Mod. Phys. B 17 (1&2) (2003) 169–172.
[60] T. Inamuro, R. Tomita, F. Ogino, Lattice Boltzmann simulations of drop deformation and breakup in shear flows, Int. J. Mod. Phys. B (2002).
[61] L. Luo, S. Girimaji, Lattice Boltzmann model for binary mixtures, Phys. Rev. E 66 (2002) 035301.
[62] H. Xi, C. Duncan, Lattice Boltzmann simulation of three-dimensional single droplet deformation and breakup under simple shear flow, Phys. Rev. E 59 (3) (1999).
[63] H. Niimura, Verification of multi-component lattice Boltzmann method, Int. J. Mod. Phys. B 17 (1&2) (2003).